Spherical bubble motion in a turbulent boundary layer

Keith Felton and Eric Loth
Department of Aeronautical and Astronautical Engineering, University of Illinois, Urbana, Illinois 61801

(Received 13 December 1999; accepted 24 May 2001)

Monodisperse dilute suspensions of spherical air bubbles in a tap-water turbulent vertical boundary layer were experimentally studied to note their motion and distribution. Bubbles with diameters of 0.37–1.2 mm were injected at various transverse wall-positions for free-stream velocities between 0.4 and 0.9 m/s. The bubbles were released from a single injector at very low frequencies such that two-way coupling and bubble–bubble interaction were negligible. The experimental diagnostics included ensemble-averaged planar laser intensity profiles for bubble concentration distribution, as well as Cinematic Particle Image Velocimetry with bubble tracking for bubble hydrodynamic forces. A variety of void distributions within the boundary layer were found. For example, there was a tendency for bubbles to collect along the wall for higher Stokes number conditions, while the lower Stokes number conditions produced Gaussian-type profiles throughout the boundary layer. In addition, three types of bubble trajectories were observed—sliding bubbles, bouncing bubbles, and free-dispersion bubbles. Instantaneous liquid forces acting on individual bubbles in the turbulent flow were also obtained to provide the drag and lift coefficients (with notable experimental uncertainty). These results indicate that drag coefficient decreases with increasing Reynolds number as is conventionally expected but variations were observed. In general, the instantaneous drag coefficient (for constant bubble Reynolds number) tended to be reduced as the turbulence intensity increased. The averaged lift coefficient is higher than that given by inviscid theory (and sometimes even that of creeping flow theory) and tends to decrease with increasing bubble Reynolds number.
 [DOI: 10.1063/1.1388051]

I. INTRODUCTION

Understanding the mechanisms that drive turbulent bubble motion can lead to better predictions of two-phase flow fields and is the motivation for the present study. However, there is a lack of knowledge as to how turbulence in wall-bounded flows controls spherical bubble trajectories, void fraction (α) distributions, and bubble forces. Studying these aspects for the specific case of a vertical turbulent boundary layer is the objective of this study.

A. Previous studies of bubble distribution

The initial work in bubble distribution focused on documenting the steady-state conditions, e.g., studies reported by Serizawa *et al.*[1] and Herringe and Davis[2] on the lateral distribution of ellipsoidal bubbles in nondilute pipe flows. More recent studies have allowed documentation of a number of flow conditions. Investigators of upward-flowing, pipe flows have observed three types of void fraction profiles: ‘‘Coring’’ (Nakoryakov *et al.*,[3] Van Der Welle,[4] Beyerlein *et al.*[5]), ‘‘wall-peaking’’ (Serizawa *et al.*,[1] Beyerlein *et al.*,[5] Michiyosi *et al.*,[6] Wang *et al.*,[7] Liu *et al.*[8]) and ‘‘saddle’’ profiles (Sekoguchi *et al.*,[9] Wang *et al.*,[7] Liu *et al.*[8]). Coring void profiles are associated with a high percentage of bubbles along the pipe centerline, while wall peaking profiles have a predominance of bubbles along the pipe wall. Saddle profiles have a nearly equal quantity of bubbles along the wall and pipe centerline. There is substantial debate as to the exact cause of wall-peaking, i.e., whether it is a product of the turbulence gradients, bubble lift forces, weak pressure gradients, bubble sizes, eddy dynamics, or a combination of these factors. This debate is complicated by the fact that most experiments have included deformable bubbles ($d_B > 1.3$ mm), significant polydispersion of bubble size, and nondilute conditions (i.e., $\alpha > 1\%$) where significant bubble-bubble interaction and turbulence modulation can occur. The study by Sekoguchi *et al.*[9] is the only dilute study for ellipsoidal bubbly pipe flows that was found in the open literature, while no equivalent dilute-flow spherical bubble studies were found.

To allow more direct insight into the bubble motion in wall-bounded turbulence, researchers have recently shifted attention to the flat plate boundary-layer where the presence of a nonturbulent far-field can simplify the underlying interactions. Experimental investigations for nonspherical bubbles ($d_B > 1.3$) include Moursali *et al.*,[10] Lance *et al.*,[11] and Tran-Cong *et al.*[12] These studies explored void fraction distribution, wall interaction, and diffusion mechanisms for deformable bubbles in a vertical turbulent boundary layer. Similar issues are explored in the present study for spherical bubbles. One of the few void fraction distributions studies for a mono-disperse bubbly flow is that of Moursali *et al.*,[10] where they introduced bubbles with a mean diameter of 3.5 mm near the leading edge of the flat plate. The void fraction was approximately 1.5%, constituting a nearly dilute flow. The results showed significant wall-peaking of the void fraction profile, where the peak tends to occur at a transverse position somewhat greater than the bubble radius ($Y_{\text{peak}}/d_B \sim 0.65$). Tran-Cong *et al.*[12] performed a similar study for a larger range of diameters but focusing primarily on trajectory distributions; they noted that the smaller ellipsoidal bubbles are more likely to migrate toward the boundary-layer plate and become trapped inside the boundary layer.

Investigations of *spherical* bubble diffusion in boundary layers are less common. Merkle and Deutsch[13] have conducted one of the few spherical bubble investigations for a flat plate flow. They studied the drag-reduction effectiveness of introducing a high concentration of micro-bubbles along a horizontal plate. They noted that the micro-bubbles tended to remain trapped inside the turbulent boundary layer, but the information on bubble trajectories and diffusion was only qualitative.

B. Bubble dynamic equation of motion

The equation of motion intended for spherical bubbles of high Reynolds number (Re_B) consistent with the present flow conditions was described by Sridhar and Katz[14] for studying spherical bubbles in a laminar vortex. This is also the same equation used by Ford and Loth[15] to study liquid forces acting on an ellipsoidal bubble in a turbulent free-shear flow. The equation equates the acceleration of the bubble mass and apparent mass with the buoyancy, fluid stress, drag, and lift forces:

$$\begin{aligned}\text{Vol}_B(\rho_B+\rho_F C_M)d\mathbf{V}_B/dt \\ =\text{Vol}_B(\rho_B-\rho_F)\mathbf{g}+\text{Vol}_B\rho_F[(1+C_M)D\mathbf{V}_F/Dt]+\mathbf{D}+\mathbf{L},\end{aligned} \tag{1}$$

where ρ_B and ρ_F are bubble and fluid density, C_M is the added mass coefficient ($=1/2$ for a sphere), Vol_B is the bubble volume$=\pi d_B^3/6$, d_B is the bubble diameter, $\mathbf{V}_B$ is the bubble velocity, $\mathbf{V}_F$ is the fluid velocity, $\mathbf{g}$ is the gravitational vector and **bold** indicates a vector. The added mass term is based on the Auton *et al.*[16] inviscid flow assumption. As noted by Maxey and Riley,[13] the stress gradient term resulting from fluid acceleration ($D\mathbf{V}_F/Dt$) includes both pressure and viscous stress gradients acting on the bubble. The Faxen and Basset history terms are neglected in Eq. (1) for the present flow conditions, consistent with relative force estimations by Sridhar and Katz[14] and Ford and Loth.[15] The formulation is also similar to that used by Spelt and Biesheuvul.[17]

The substantial derivatives along the bubble path and fluid path in the above equation of motion are defined as

$$\frac{d}{dt}(\quad)=\frac{\partial}{\partial t}+\mathbf{V}_B\cdot\nabla(\quad), \tag{2}$$

$$\begin{aligned}\frac{D}{Dt}(\quad)&=\frac{\partial}{\partial t}+\mathbf{V}_F\cdot\nabla(\quad)\\ &=\frac{d}{dt}(\quad)-(\mathbf{V}_B-\mathbf{V}_F)\cdot\nabla(\quad).\end{aligned} \tag{3}$$

The lift and drag forces to be measured can be written in terms of their coefficients as

$$\mathbf{D}=(\tfrac{1}{2})C_D\rho_L S_B|\mathbf{V}_{\text{rel}}|\mathbf{V}_{\text{rel}}, \tag{4}$$

$$\mathbf{L}=(\tfrac{1}{2})C_L\rho_L S_B|\mathbf{V}_{\text{rel}}|^2(\mathbf{V}_{\text{rel}}\times\omega_F)/|\mathbf{V}_{\text{rel}}\times\omega_F|, \tag{5}$$

where C_D is the quasi-steady drag coefficient, C_L is the quasi-steady lift coefficient, $\mathbf{V}_{\text{rel}}$ is the bubble velocity relative to the surrounding fluid such that $\mathbf{V}_{\text{rel}}=\mathbf{V}_B-\mathbf{V}_F$, ω_F is the local vorticity vector, and S_B is the bubble projected area ($=\pi a_B^2$).

C. Previous studies of drag and lift of spherical bubbles

Limited information is available in the open literature regarding forces that act on spherical bubbles as they move through a turbulent flow field.[18] Most of the previous investigations have focused on the drag forces on rising bubbles in a quiescent flow, e.g., Clift *et al.*[19] The results have generally shown that the drag force coefficient of small spherical bubbles in quiescent tap water is comparable to that of rigid spheres. This is consistent with an approximate no-slip condition resulting from contamination typically found in tapwater which serves to immobilize the bubble surface. Sridhar and Katz[14] found such results for $20<\text{Re}_B<85$ for recent experiments of bubbles in a laminar vortex flow, whereupon the following solid-particle drag expression was found to be satisfactory:

$$C_D=(24/\text{Re}_B)(1+0.15\,\text{Re}_B^{0.687}), \tag{6}$$

where $\text{Re}_B=|\mathbf{V}_{\text{rel}}|d_B/\nu_F$, and ν_F is the kinematic fluid viscosity. However, in turbulent flows the mean relative rise velocity has been observed to differ significantly from that in quiescent flow conditions with both increases and decreases observed.[20,21] This result may stem in part from effects of turbulence on the drag coefficient relationship (the subject of this study). To date, there have been no measurements of the instantaneous C_D as a function of Re_B for a spherical bubble of fixed diameter in varying levels of turbulence.

For the shear lift force on spherical bubbles at $\text{Re}_B \gg 1$, there are some relevant theoretical and experimental results. Auton *et al.*[16] have analytically studied the lift force based on a potential flow model and found it is proportional to the local vorticity such that lift can be represented as

$$\mathbf{L}=-\tfrac{1}{2}\rho_F\text{Vol}_B\mathbf{V}_{\text{rel}}\times\omega_F. \tag{7}$$

This is substantially different than the creeping flow theory, which yields a lift in the same direction but of magnitude

$$L=1.61\rho_f V_{\text{rel}}d^2(\nu_f\omega_F)^{1/2}. \tag{8}$$

A limited number of direct lift force measurements have been reported for *free* spherical bubbles and particles for high-Reynolds numbers. Naciri[22] conducted one of the first bubble lift force experiments for $20<\text{Re}_B<120$, by computing the forces from the equilibrium position of bubbles within a rotating cylinder containing water. The C_L data substantially exceeded Auton *et al.*[16] results and also showed a decrease with increasing Reynolds number for a constant nondimensional vorticity ($d_B\omega_F/V_{\text{rel}}$). For Re_B of 10–40, it was asserted that this reduction was proportional to $\text{Re}_B^{-1/2}$, similar to the trend for creeping flow theory. However, the

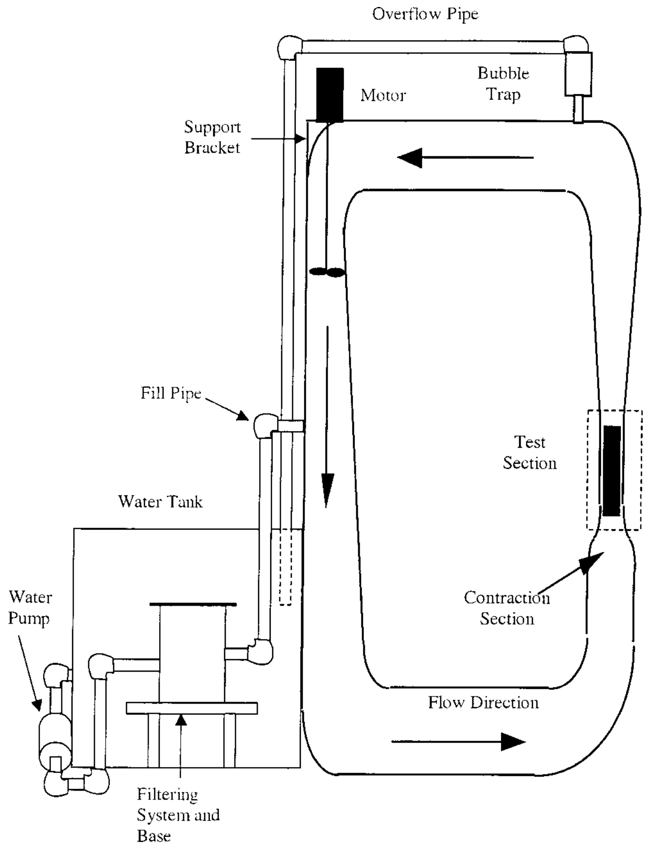

FIG. 1. Schematic of closed-loop water tunnel used to create vertical turbulent boundary layer.

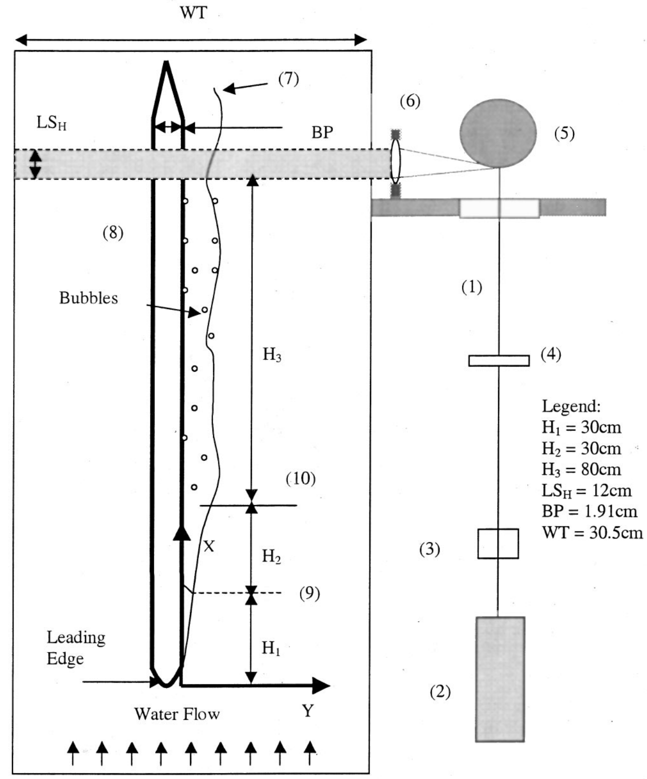

FIG. 2. Schematic of boundary layer plate and optical arrangement of the laser sheet with respect to field of view. The incoming beam (1) for the laser sheet projection is produced via a 5W Argon-Ion laser (2), beam directing mirror (3), focusing lens (4), 24-sided scanning mirror (5), and collimating lens (6). The turbulent boundary layer (7) is established by the boundary layer plate (8), and tripping mechanism (9). The bubble injector (10) could be traversed horizontally (normal to the boundary layer plate).

experimental uncertainty may have been too significant to quantitatively conclude the power relationship. Sridhar and Katz[14] explored the lift forces acting on 500–800 μm diameter spherical bubbles entrained in a laminar vortex. They found that the experimental lift force exceeded both the creeping flow and the inviscid theory and in their case approximately scaled with the fourth root of the nondimensional vorticity but did not find a consistent correlation with Re_B. Numerical predictions of lift forces in shear for stationary particles and bubbles at finite Reynolds number, e.g., Mei and Klausner[23] and Legendre and Magnaudet[24] generally yield magnitudes equal to or less than the inviscid limit for $\mathrm{Re}_B > 40$ and thus significantly underpredict the above experimentally observed behavior. This is potentially due to the fact that the numerical particles are computationally fixed with respect to spin and velocity, i.e., they are not "free."

II. EXPERIMENTAL METHODS

A. Flow facility

The dynamics of millimetric air-bubbles inside a vertical, wall-bounded liquid shear layer were experimentally investigated in this study. The experimental facility is located in the UIUC Hydrosystems Laboratory and consists of a closed loop water tunnel (Fig. 1). The tunnel volume is approximately 4500 liters, with a passive bubble trap located at the top of the water tunnel to eliminate bubble recirculation. In the water tunnel test section, a boundary layer plate, bubble injection system, and Particle Image Velocimetry (PIV) system were installed (Fig. 2). Details of the set-up may be found in Felton.[25] The spanwise width and depth of the test region are 30 cm each, providing sufficient spanwise and transverse distance to ensure negligible wall effects in the test interrogation region. The flow field's boundary layer was produced as a result of the upward flowing wall-bounded liquid at velocities from 0.4 to 0.9 m/s, and the resulting flow conditions are listed in Table I.

In order to ensure a turbulent flow, the present boundary layer employed a tripping device, which consisted of a series of spanwise delta wings fixed to the plate and set at angle of attack to the incoming flow. The resulting delta wings, at a height of approximately 4 mm, were located 30 cm downstream of the leading edge. This streamwise location and tripping device height were selected to ensure that fully turbulent flow conditions began immediately downstream of the roughness location, per the method of Braslow *et al.*[26] This

TABLE I. Summary of the flow field conditions.

Case	U_o (m/s)	δ (mm)	Re_δ
LR	0.4	33	13 000
MR	0.6	28	17 000
HR	0.9	22	20 000

experimental technique is commonly used for airfoil trip strips in order to obtain a rapid transition from laminar flow to turbulent flow, since a very short transition length is a favorable attribute for aerodynamic computational methods. The tripping technique is primarily based on the roughness Reynolds number, whereby a value of 300 or more is suggested, and a minimum value of 650 was used in the present study. Details of the criteria and roughness features are given in Felton.[25]

The tap water in the tunnel was filtered (prior to seeding with PIV tracers) through filter papers with a 2.5 micron pore size. This filtration was necessary to eliminate any particulates with diameter on the order of the seeding particle size of 8 microns. No other water treatment was employed, such that the immobilization of the liquid–gas interface caused by natural contaminants is expected to be approximately consistent with other ''tap water'' experiments.

B. Bubble generation system

This bubble generation system consisted of a 0.005 liter syringe tube, a hypodermic needle, a syringe pump, an EFT valve, and a compressed air tank based on the single-bubble injection technique of Park *et al.*[27] However, the present set-up differs in that an additional pressure line was added to the syringe to allow multiple injections without draining the water tunnel. The compressed air was delivered through various hypodermic needles with injection tip sizes of 22, 26, 28, 30, and 32 gauge used to produce monodisperse bubble diameters of 370–1200 μm inside the turbulent boundary.

A high precision Cole–Parmer (model E 74900-00) syringe pump with a rated accuracy of $\pm 0.5\%$ was used to produce the air for the bubbles. A flow rate of 2 to 3 ml/hr was chosen for the measurements presented herein. This rate was chosen to obtain very low mean void fractions ($\sim 3 \times 10^{-5}$) in the boundary layer test region to ensure negligible bubble–bubble interactions and negligible turbulence modulation for all conditions. This rate was necessary because void fractions as low as 10^{-4} for some of the present wall-peaking conditions resulted in occasional bubble coalescence which invalidated the mono-disperse bubble distribution needed for this study.

Bubble sizing for each test was conducted with a separate high-magnification camera, which was validated with spherical glass beads (0.3–1.0 mm) in the test section. For quiescent flow, bubble diameters were consistent with the bubble release volume estimates of Oguz and Prosperetti,[28] but were reduced as the upward liquid velocity increased. The maximum diameter uncertainty was 3.6% and the maximum standard deviation for the diameter distributions was $\pm 4.7\%$.

The transverse (horizontal) bubble injection location (Y_{inj}/δ) was varied over a range of 0.1–1.2, where δ is the field-of-view boundary layer thickness. The vertical injector exit position was located 80 cm upstream of the laser field of view. Since air bubbles in water achieve their terminal velocity in less than a centimeter, the injector location assured that the bubble motion in the field of view was essentially independent of their formation at the injector and the location allowed significant diffusion to occur. In addition, the wake of the thin 0.72 mm OD injector tube is expected to have a negligible impact on the downstream boundary layer development and structure.

C. Bubble distribution technique

Measurements of the bubble population concentration were obtained using a laser intensity methodology[29] by employing basically the same laser and lens PIV optics for illumination but without the 8 μm tracer particles and with long-exposure photography. The interrogation region (for bubble distribution and PIV) was fixed over the stream-wise range of $X = 140–147$ cm and the bubble injection point was at $X = 60$ cm. This method allows one to record individual bubbles as they move through the test interrogation region by tracking its location at every laser sweep. The tracking of several hundred bubbles over a long time period for each condition yielded statistically sufficient bubble population distribution measurements. This technique was accomplished in three stages: (1) Long-exposure photography, (2) digitization, and (3) data reduction.

The images of the bubble trajectories in the test interrogation region were acquired using a 35 mm Canon T-90 camera equipped with a 100 mm $f^{\#}$ 4.5 macro lens, 12 mm extension tube, and a 60 second shutter speed (i.e., sampling time) for observing the bubble distribution. Twenty-five to thirty photographs were recorded on Kodak TMAX-400 black and white film for each test condition and processed with the standard TMAX-400 guidelines. This yielded a total sample time of 25–30 minutes per test run and the net acquisition of thousands of bubble images. This net acquisition time was found to yield statistically stable and reproducable results. The film negatives were digitized using the high-resolution Studio Scanner II at 800 ppi (further increases in resolution yielded insignificant changes in the results). A scanned background photograph (with no bubbles) was subtracted from each bubbly flow photograph, which were then thresholded.

The twenty-five to thirty resulting digital images for each test condition were then ensemble-averaged and then row-averaged to determine the intensity along pixel columns normal to the boundary layer. Each row represented the transverse bubble concentration for a discrete streamwise position in the laser sheet. The resulting distribution was equated to the local bubble number concentration, which in turn is proportional to the void fraction distribution (α) for monodisperse bubbles. The intensity was then normalized by the peak value for each distribution. Generally, the void fraction peak ($\alpha/\alpha_{\max}=1$) was found to be reproducible to within 5% of δ (and within 2% of δ when the peak was near the wall). This image intensity method was independently validated with a transverse bin method where all individual bubble images were hand-counted to alternatively obtain the mean bubble number distribution. The comparison indicated a void peak location uncertainty for the image intensity method of less than 5% of δ. The orientation of the horizontal bubble injector was found to have negligible influence. In particular, the peak void fraction exhibited a difference of less than 0.01δ for the injector pointed towards the wall vs pointed in the spanwise direction. This indicates that any initial horizontal bubble velocity was not important to the downstream test section void distribution.

D. Cinematic particle image velocimetry system

For the PIV images, the water tunnel was seeded with 15–20 ml of 8 μm diameter clear glass spheres (specific gravity = 1.1) manufactured by Potters Industries. The particle concentration was approximately 0.002 grams/liter which is enough to ''contaminate'' the water but an order of magnitude below the minimum value which denotes ''grossly contaminated'' systems.[30] Thus, the seed addition is not expected to have a significant effect on the level of contamination beyond that already given by the natural contaminants. As evidence of this, the terminal rise velocity of both ellipsoidal and spherical gas bubbles in the tap water were measured with and without the seed particles, with no significant difference found in either case. Notably, the viscosity of the tap water which was filtered and seeded was 1.07 cP at 18.3 °C as compared to 1.05 cP for pure distilled water (and 1.09 cP for the unfiltered unseeded tap water).

The PIV optics and camera are comprised of a Spectra-Physics 5W Argon-Ion Laser, 24-sided Lincoln Laser rotating mirror, and various lens and mirrors designed to steer and focus the laser beam.[15] The rotating mirror has a variable frequency range of 5–50 Hz, and it is coated with an Al–SiO reflective coating with a surface flatness of 1/4 wavelength. Precise machining, and assembly ensured that the mirror surfaces are parallel to the rotating axis, which is critical to produce identical laser scanning sheets. The rotating mirror frequency was set to produce four sweeps for each film frame. The use of multiple sweeps effectively increases the particle seeding density and signal to noise ratio of the particle-displacement peaks.[31] Following the rotating mirror is a 145 mm diameter collimating lens with a 250 mm focal length. It is designed to produce a beam sweep of 122 mm. A measurement and estimate of the beam thickness shows a 1 mm thick beam is projected into the interrogation region.

The multiple-pulse images of the seed particles and bubbles were then recorded with a movie camera at 30 fps to allow temporal resolution. The Mitchell 35 mm variable-speed movie camera was equipped with double-pin registers for high film stability, and a 60 mm Nikor macro lens for high resolution.[15] Velocity interrogations for the turbulent boundary layer were performed using a TSI Model 6000 PIV Analysis System (version 3.6). A single-frame auto-correlation technique was applied to square interrogation spots on the film, which producing a physical vector spacing of 2.2 mm, using 50% overlap. The vector spacing was about 2.2 mm, which on average corresponds to about 8% of δ. This spacing is coarse with respect to the bubble size (the diameter ranges from 1% to 5% of δ) and especially with the mean Kolmogorov scale (which is approximately 1% of δ), but the vector spacing is approximately consistent with the Taylor microscale (which is estimated to be about 10% of δ). A matrix of 21 (transverse) by 31 (streamwise) liquid velocity vectors (V_F) was thus obtained for each movie frame. Computing the circulation over adjoining vectors, the liquid vorticity could also be calculated. The velocity uncertainty analysis took into account finite film and CCD resolution, uncertainty of the scanning mirror speed, and the temporal variation of laser sweeps for a given particle sweep-wise velocity (Oakley *et al.*[32]). This analysis revealed a maximum instantaneous liquid velocity uncertainty within the boundary layer of less than 2% of U_O (freestream speed) and a maximum instantaneous vorticity uncertainty of less than 30% of U_O/δ (where δ is the boundary layer thickness). This cinematic PIV technique was used both to document the single-phase flow characteristics and also to determine the bubble forces (as described below).

E. Bubble force measurements

The bubble force technique is similar to that given by Ford and Loth[15] and will be described briefly below. Once the velocity vector maps were obtained from the PIV interrogations, the locations of the bubbles were individually selected by examining sequences of the movie film for high-clarity trajectories. All bubbles selected were at least ten bubble diameters from their nearest neighbors (in general, only one bubble was in the field of view at a time). The positions of the bubble images were obtained by using the same CCD camera and monitor used in the PIV interrogations. Using a Unidex motion controller with micron movement allows for precise location of these points. The coordinates for the bubbles in the boundary layer were then plotted as functions of time (x and y vs t) using seventh-order polynomial curve fits. Then, these curve-fits were differentiated to give the x and y components of bubble velocity ($\mathbf{V}_B$) and acceleration ($d\mathbf{V}_B/dt$). The uncertainty in the bubble velocity was estimated to be less than 5% of the terminal velocity of the bubble. The coordinates of the instantaneous bubble position were also used to obtain the surrounding liquid velocity by interpolation of the values from the surrounding four velocity vectors (spaced at about two–six times the bubble diameter). The acceleration of the liquid ($d\mathbf{V}_F/dt$) is then evaluated at discrete times for each frame again using the seventh-order curve fits. The $\nabla(\mathbf{V}_F)$ term contains the spatial gradients of the liquid velocity calculated from central differences on the surrounding grid points, and then interpolated at the bubble location. Note that the resulting errors in liquid acceleration interpolated to the bubble location are significant, e.g., 25%.

Once the time-varying liquid velocity and vorticity fields, the bubble diameter, and the history of the bubble position, velocity and acceleration were obtained, Eq. (1) can be solved directly for instantaneous forces of drag (**D**) and lift (**L**) by using Eqs. (4) and (5). The total uncertainty of the resulting force coefficients is briefly described in the following, and is similar to that discussed in Ford and Loth.[15]

For buoyancy-dominated conditions, the measured drag coefficient is proportional to $d_B g/(V_{\mathrm{rel}}^2)$ based on Eqs. (1) and (4). The uncertainty for V_{rel} is simply obtained by combining the uncertainty of V_B and V_F. The total error based on pixel resolution for V_F is the sum of the bias error and the random error, where the latter dominates for the present conditions and is highest for the velocities close to the wall. At these conditions the minimum pixel displacement is about 22 pixels, and when combined with the pixel accuracy of 0.2 mm and a laser sweep speed of 120 Hz, yields an uncertainty of 1.1 mm/s for the lowest speed flow. However, one must consider the error associated with linearly interpolating the velocity (measured at a point) to the velocity at the bubble location, which is a maximum interpolated transverse distance ($\Delta Y_{\rm int}$) of 1.1 mm. The spatially filtered error for the linear velocity variation can be approximated as the second-order truncation term: $(d^2V_F/dY^2)\Delta Y_{\rm int}^2$. Approximating the second derivative with the ratio of wall-friction velocity to the square of the Taylor-microscale yields a filtered velocity error of roughly 2.0 mm/s, which is 4% of the smallest terminal bubble velocity. These values can be combined with the bubble velocity uncertainty to yield an uncertainty of 9% for $V_{\rm rel}$. This can be further combined with the uncertainty due to bubble size, to yield a maximum drag coefficient uncertainty of 22%. However, this neglects the effects of uncertainties in dV_F/dt and dV_B/dt which arise via (1) and are considered in the following.

To include the effects associated with liquid acceleration uncertainty, we note that this term is proportional to $d_B(DV_F/Dt)/V_{\rm rel}^2$ when compared to the drag coefficient based on (1) and (4). The maximum liquid accelerations observed by Felton[25] at the PIV interrogation points are about 10% of g (e.g., Fig. 13), and the corresponding uncertainty when interpolating the liquid acceleration to the bubble location is about 3% of g. The uncertainty for the bubble acceleration is also about 3% of g. Therefore, the overall estimate of drag coefficient uncertainty is about 30%. Because of this, many instantaneous measurements (e.g., 20 data points) were taken to establish each drag coefficient curve as a function of Reynolds number (which itself has an average uncertainty of 13%).

The instantaneous lift force uncertainty has the same dimensional dependence on uncertainties in bubble size, and is also affected by errors in liquid and bubble velocity–acceleration by examination of Eqs. (1) and (5). However, since C_L values are typically an order of magnitude smaller than C_D values, the relative uncertainty of instantaneous lift coefficient is much higher than for the drag coefficient. Therefore, twenty to thirty instantaneous bubble lift measurements were averaged at two transverse location ($Y/\delta \sim 0.5, 1.0$) to obtain averaged lift coefficients, $\overline{\mathbf{C}}_L$, for which the relative uncertainty is estimated to be 50%. These averaged lift coefficients were then compared to the nondimensional *average* vorticity values ($\omega d_B/V_{\rm rel}$), for which the uncertainty was estimated to be about 20%.

III. RESULTS

A. Single-phase flow field

Three free stream velocities ($U_o = 0.4, 0.6, 0.9$ m/s) were employed in this study and investigated with the PIV technique.[15] The purpose of these measurements is to demonstrate that the boundary layer is indeed turbulent. We present herein results for the lowest Reynolds number case (13 000), since it was the limiting condition for the establishment of the turbulent boundary layer. Representative velocity statistics were obtained by from thirty-five randomly selected PIV images and streamwise averaging (yielding over 1000 data points to describe transverse variations). Conventional statistical analysis indicated an accuracy for the mean velocity of less than 2% of U_o whereas the accuracy for the rms velocity fluctuations was about 10% of the peak value.[25] Figure 3 depicts the mean streamwise and transverse velocity profiles for the low-Reynolds number (LR) case ($\mathrm{Re}_\delta = 13\,000$). The streamwise velocity distribution was found to be in accordance with previous low-Reynolds flat-plate turbulent boundary layers studies.[33–35] The transverse velocity profile normalized by the freestream is limited to a few percent of U_o for $0.0 < y/\delta < 1.0$. Figure 4 depicts the streamwise and transverse turbulence distributions, which are also consistent with other low-Reynolds boundary layers.[34,35] The variations between the present data and that of Meinhart and Tomkins may be related to differences in the turbulent tripping techniques used. The present flow has a trip device located at $\mathrm{Re}_x = 1.2\times10^5$ to obtain rapid transition, whereas the latter two studies by Meinhart[33] and Tomkins[35] used a trip strip (roughness surface) located at the leading edge. Results by Klebanoff[36] were at a higher Reynolds number ($\mathrm{Re}_\delta = 75\,000$) such that no artificial trip was required and are reasonably consistent with the present data. However, it should be noted that the flat plate boundary layer of Moursali *et al.*[10] ($\mathrm{Re}_\delta = 19\,000$) used an abrasive ribbon as a transition strip at the leading edge of their plate but found turbulence intensities which were slightly lower than those reported herein. As such, some variation in turbulence intensities is expected at these low-Reynolds numbers, but in general the present flowfield is reasonably consistent and can be re-

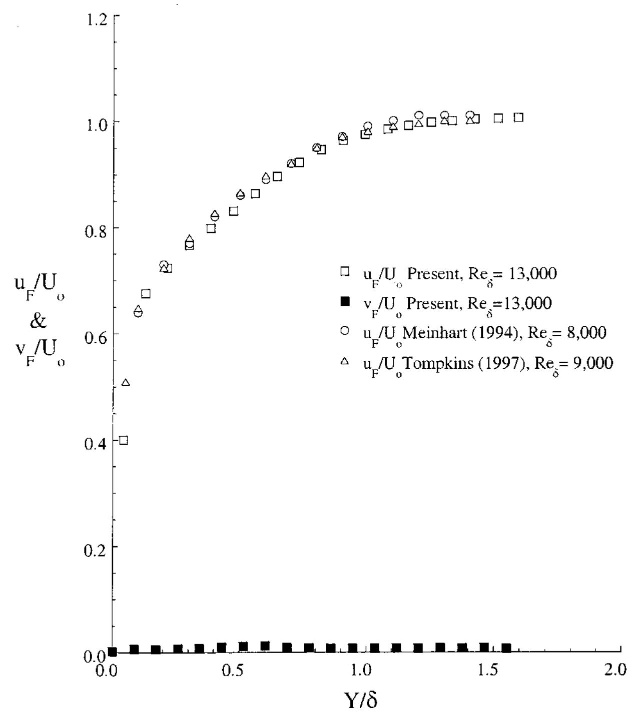

FIG. 3. Nondimensional mean velocity distribution as a function of transverse location based on 35 randomly selected PIV frames.

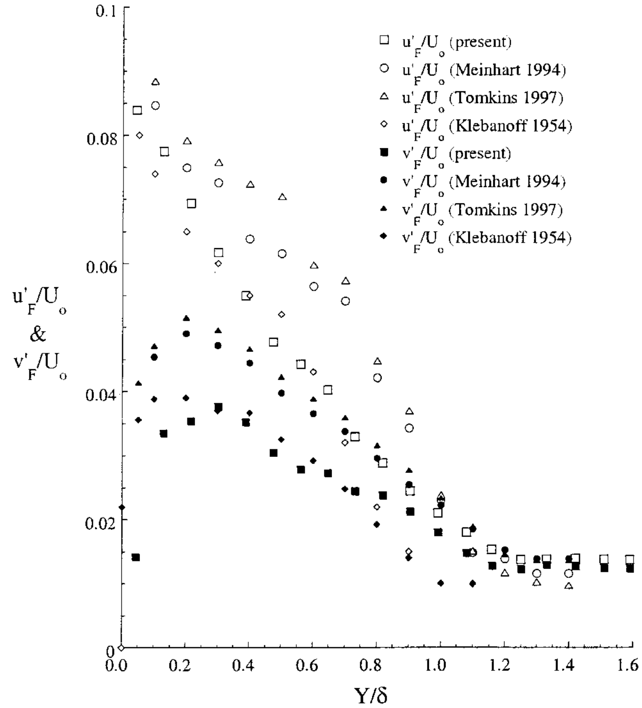

FIG. 4. Turbulence level vs nondimensional transverse position for 35 randomly selected PIV frames.

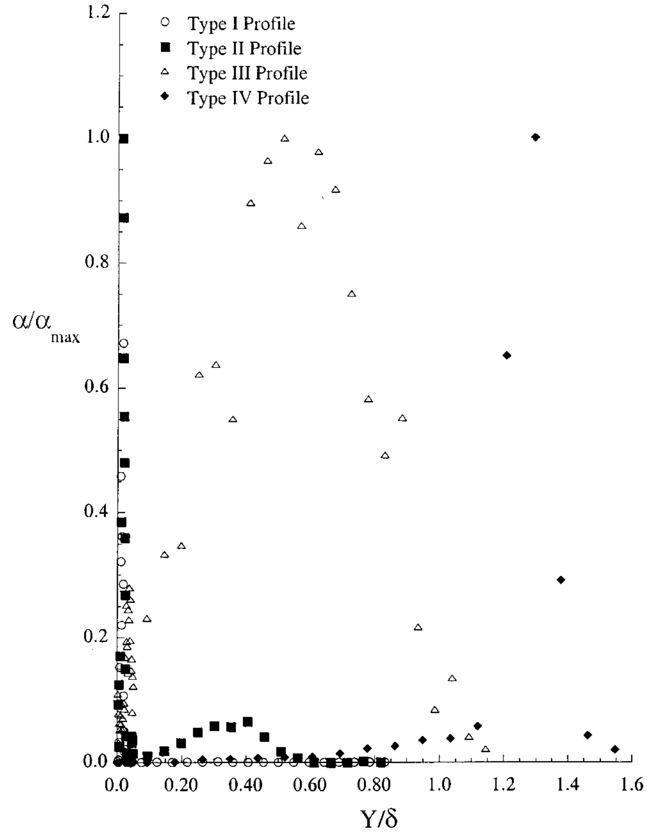

FIG. 5. Representative bubble concentration distributions observed in this study.

garded as turbulent. The addition of bubbles to the flow (at the void fractions of the present study) yielded PIV statistics with a negligible difference from their single-phase counterparts.

B. Void fraction distribution in turbulent boundary layer

For the test conditions of the present study, four distinct bubble distribution profiles were identified, and they are classified as types I–IV profiles. An example of each profile is shown in Fig. 5. Type I profiles resulted in almost all bubbles trapped along the wall (with little or no bubble drift away from the wall), i.e., a single monotonic spike in the void fraction distribution at $Y \ll \delta$ as shown by the open circle data points in Fig. 5. Type II profiles exhibited a high concentration of bubbles trapped along the wall (similar to type I) as well as a significant portion of bubbles dispersing away from the wall, i.e., a monotonic spike in the void fraction distribution at $Y \ll \delta$ as well as a secondary peak typically between $0.3 < Y/\delta < 0.5$, as shown by the solid square data points in Fig. 5. Type III profiles exhibited bubble dispersion throughout the boundary layer with a concentration peak near the transverse injection point. Type IV profiles yielded bubble trajectories primarily along the mean boundary layer edge. Of the four, the type III void fraction profiles tended to cover the largest fraction of the boundary layer thickness and were characterized by a Gaussian-type transverse distribution. The net transverse bubble distribution thickness was small in comparison to the total streamwise diffusion length (e.g., 1%) which is consistent with the growth rate of the turbulent boundary layer in that same streamwise section.

The void fraction profiles were investigated to examine effects of injection location, eddy Froude number (ratio of hydrodynamic pressure gradients to hydrostatic pressure gradients), Stokes number (ratio of bubble response time to eddy turnover time), and drift parameter (ratio of terminal velocity to turbulence intensity). In general, as the Stokes number decreased (while other parameters were held constant) the profile type moved from a Type I to a Type II, and then to a Type III, i.e., a transition away from the wall. This type of trend was also observed as the injection point location was increased (while other parameters were held constant), e.g., Fig. 6. Increasing Froude number (and Reynolds number) did not significantly affect the void peak location.

The void profile distribution type tended to correlate best with the bubble Stokes number and injector location as shown in Fig. 7. Herein, the Stokes number is defined as the ratio of bubble response time to an integral boundary layer time scale

$$\mathrm{St} = C_M V_{\mathrm{term}} U_o / g\delta, \qquad (9)$$

where U_o is the free stream velocity and V_{term} is the terminal rise velocity. When the four void distribution profiles are compared with Stokes number and the bubble injection location, four parameter regions containing similar profiles are formed (Fig. 7). Low-Stokes number and injection values within δ generally produced type III profiles (peaks inside the boundary layer with few bubbles near the wall). Higher Stokes number conditions yielded type I (where most of the

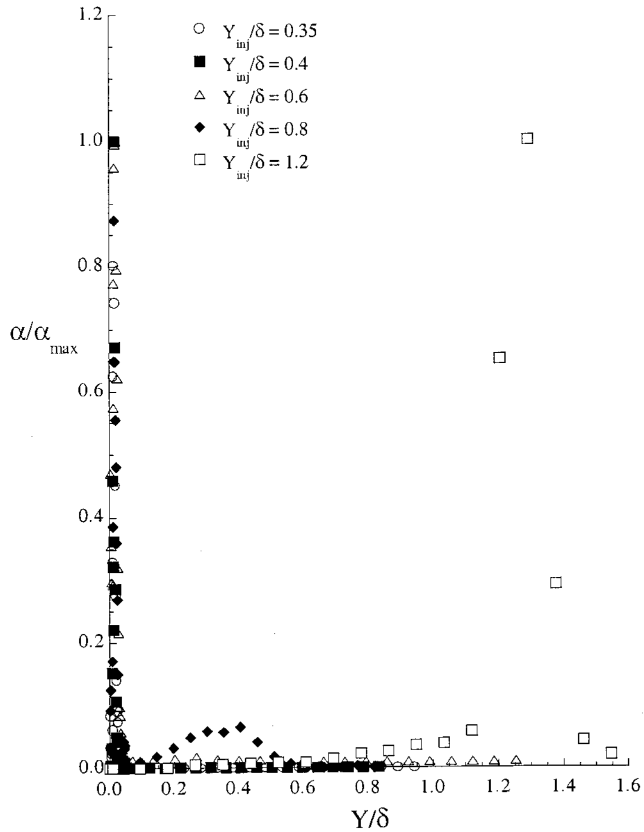

FIG. 6. Bubble concentration distributions for fixed $\mathrm{Re}_\delta(13e3)$ and St $(5.6e\text{-}2)$ for varying Y_{inj}/δ values.

bubbles collect along the wall) when injected within $\delta/2$. Type II profiles (wall peaking and secondary peaking away from the wall) occurred when similarly sized bubbles were injected between $\delta/2$ and δ. For bubbles introduced at a transverse position greater than the boundary layer thickness, the resulting profiles are primarily type IV (peaking beyond δ).

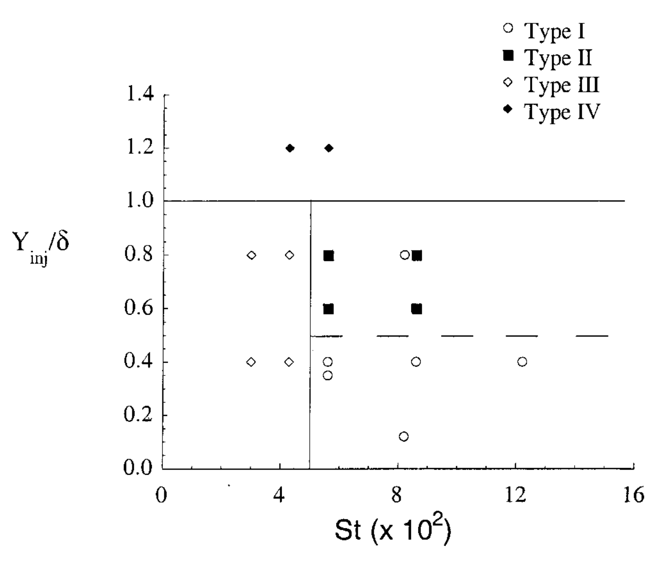

FIG. 7. Comparison of nondimensional injection points $(Y_{\mathrm{inj}}/\delta)$ vs Stokes number. Note that the Type II profiles at an injection location of 0.6 indicated only a minor peak away from the wall, i.e., were not strongly dissimilar from type I profiles.

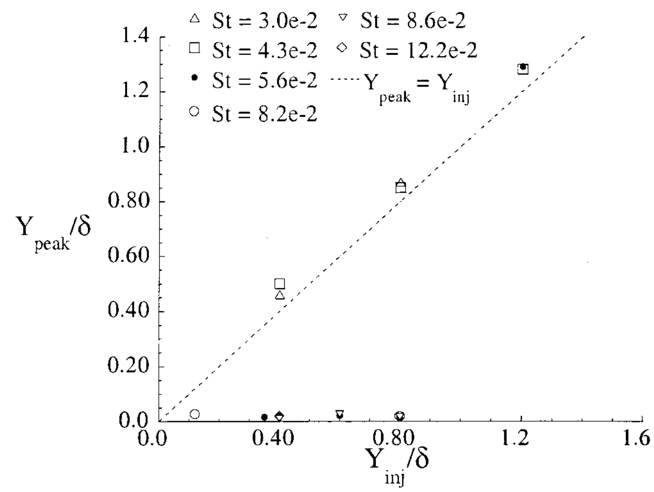

FIG. 8. Comparison of the peak bubble-concentration location vs the bubble injection location (both scaled by the boundary layer thickness) for various Stokes numbers.

While the above results simply describe an empirical correlation, the physical mechanisms for the above correlations can be considered. In previous studies of free shear flows, particles or bubbles of $\mathrm{St} \ll 1$ tend to yield turbulent diffusion consistent with that of a passive scalar, whereas larger St values are typically associated with reduced diffusion rates.[18] In the present flow, as St decreased (typically smaller bubble diameters), the bubbles diffused over a larger region of the boundary layer.[25] Conversely, the phenomenon of trapped bubbles along the wall (with little diffusion) for the present results was typical for the higher Stokes number conditions. This suggests that once spherical bubbles become very small, they tend to diffuse throughout the boundary layer as a passive scalar whereas larger bubbles diffuse less. In addition, the larger bubbles can be subjected to higher relative lift forces that can drive them to the wall. This trend of the larger bubbles collecting along the wall is also consistent with a numerical pipe flow study of spherical bubbles by Beyerlein *et al.*[5] (which they attributed to the increase in bubble relative velocity). This wall-peaking effect is also consistent with experimental studies of spherical solid-particle boundary-layer.[30] In contrast, when ellipsoidal bubbles were investigated in the experimental boundary layer study by Tran-Cong,[12] the smaller bubbles were more likely to be trapped than larger ones (the difference may be related to the bubble deformation which can cause lift direction reversal[17]).

Figure 8 quantifies the void peak locations for all four types of profiles, where it is noted that there are two distinct regimes: one for the Types II and IV profiles and one for the Types I and II profiles. The void peak $(Y_{\mathrm{peak}}/\delta)$ and the dimensionless bubble injection $(Y_{\mathrm{inj}}/\delta)$ are roughly equal for types III and IV profiles indicating that the mean drift of the bubble cloud toward the wall for $y/\delta > 0.4$ is small. This

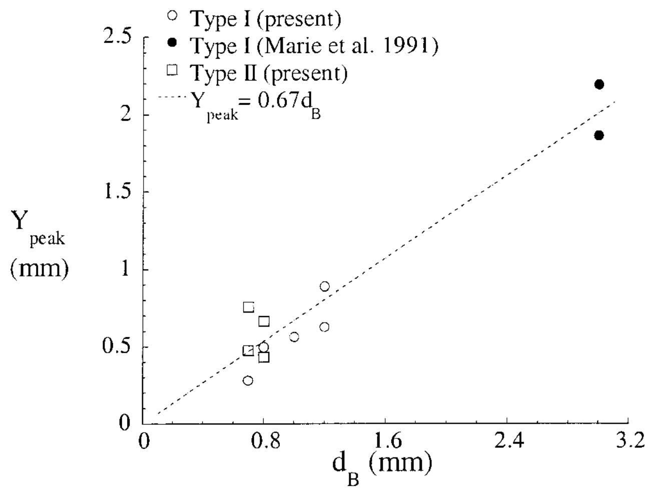

FIG. 9. Comparisons of transverse void-peak location for types I and II profiles and type I profiles from Marie *et al.* (1991).

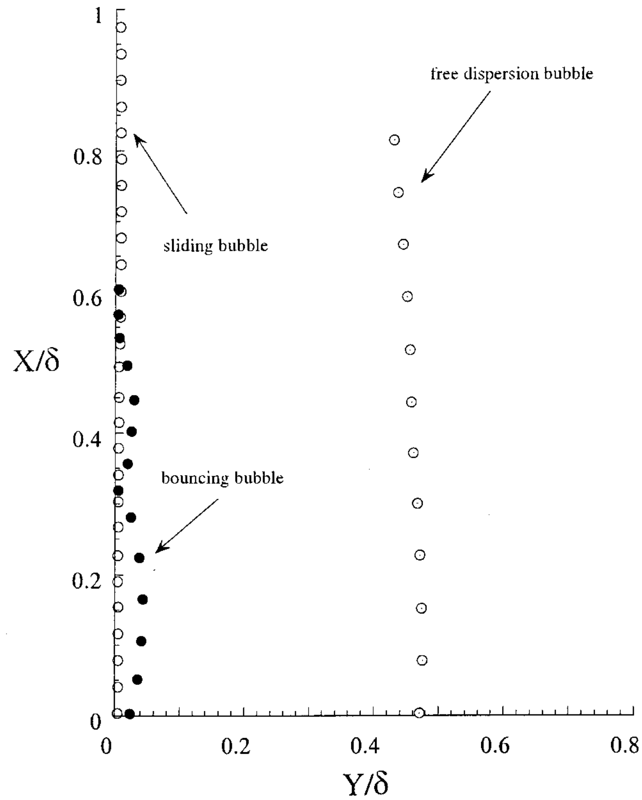

FIG. 10. Sample of millimetric bubble trajectories observed inside the vertical liquid turbulent boundary layer. Three distinct trajectories were observed: (a) free dispersion bubble, (b) bubble bounce, and (c) bubble slide.

is consistent with the lower mean vorticity in this region, such that lift does not play a significant role in the mean trajectories. In fact there is a small deviation from the Y_{inj} point away from the wall, which may be related to the mean transverse velocity. Based on a rough estimate for the mean transverse velocity in the middle of the boundary layer (averaged from bubble injection to the field of view), the net shift for a passive scalar would be about 12% of δ, which is of the order of the 8% shift observed in this figure. Figure 8 also shows that the void peak locations for type I and II profiles (mostly $\mathrm{St}>0.05$) are very small and essentially independent of the Y_{inj}/δ value. These are cases where most of the bubbles collect along the wall.

Figure 9 provides further insight into the scaling of these small void peak locations with respect to bubble size. Similar to previous ellipsoidal bubble investigations by Serizawa *et al.*[1] for pipe flow and Marie *et al.*[37] for a flat plate, the peak for the present study is located somewhat more than a mean bubble radius away from the wall ($Y_{\mathrm{peak}}/d_B \sim 0.67$). This condition suggests that a thin layer of fluid exists on-average between the wall and bubble as it slides along the plate. This result is also qualitatively consistent with experiments for 100 micron glass particles "trapped" at $Y_{\mathrm{peak}}/d \sim 0.65-0.87$ in a water pipe flow of Reynolds numbers ranging from 12 700 to 18 700 by Young and Hanratty.[30] The later study suggested that this trapping phenomenon was caused by a balance of the wall displacement force and the Saffman lift force, from which they predicted much closer equilibrium locations of $Y_{\mathrm{peak}}/d_B \sim 0.52-0.56$, i.e., with a mean separation distance from the wall of only 0.02–0.06 d_B. As such, their wall displacement force description can not conclusively explain the present results as the magnitude is not quantitatively consistent. The experimentally observed standoff distance may also be influenced by film lubrication or minor bubble excursions caused by the wall turbulence which may then lead to a set of bubble bounces (discussed in the next section).

C. Bubble trajectories

By analyzing the bubble trajectories individually, three highly distinguishable trajectories were observed: (a) bubbles sliding along the wall, (b) bubbles bouncing along the wall, and (c) bubbles freely dispersing in the boundary layer. The three types are shown with sample trajectories in Fig. 10, where the bouncing bubbles typically became trapped at the wall further downstream. One of the dramatic differences between the trajectories of various bubble sizes is that the motion of smaller bubbles ($d_B<0.6$ mm) was primarily limited to free dispersion. Conversely, the large bubbles ($d_B>0.8$) exhibited all of the observed bubble trajectories—slide, bounce, and free dispersion. This is consistent with wall void-peaking noted primarily for the larger bubbles.

The individual bubble migration to the wall in the context of the surrounding instantaneous liquid flow field was also considered (and later used for computing bubble forces as described in the next section). Figures 11 and 12 show the velocity vectors and spanwise vorticity fields for a 0.42 mm bubble trajectory which is moving towards the wall (typical of a bubble which will eventually be "trapped" along the wall) in the boundary layer of $U_o=40$ cm/s. The bubble transverse movement is substantial, i.e., moving from $Y=12$ mm to $Y=9$ mm in two frames (66 ms), yielding a transverse velocity of about 4 cm/s (quite significant when compared to the relative streamwise velocity of 7 cm/s). The rapid bubble side movement in this case is unlikely to be

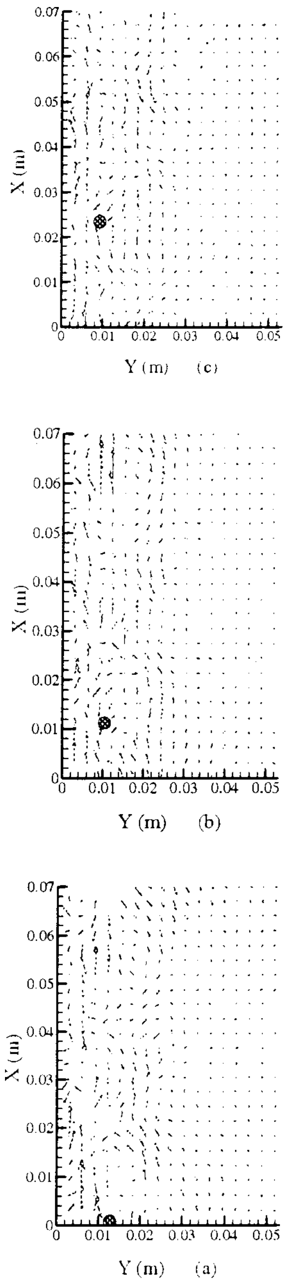

FIG. 11. Three consecutive PIV frames for a 0.42 mm diameter bubble immersed in a liquid flow field, with $U_o=0.4$ m/s, $\mathrm{Re}_\delta=13\,000$.

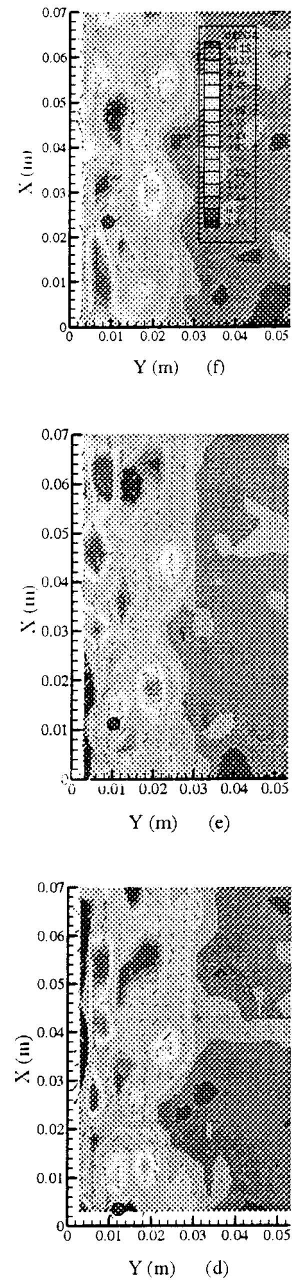

FIG. 12. Corresponding vorticity contour maps for the three consecutive PIV frames shown in Fig. 10 (0.42 mm diameter bubble with $U_o=0.4$ m/s, $\mathrm{Re}_\delta=13\,000$).

caused by drag since the local relative transverse liquid velocity coupled with a standard drag coefficient is too small to cause such a velocity and indeed the drag force would act in the opposite direction in this case. In general, the liquid transverse velocities for bubble migration were also much too small to cause the rapid wall attractions experimentally observed (recall the mean and fluctuation liquid transverse velocities have respective peak values of only $0.02U_o$ and $0.04U_o$ as shown in Figs. 3 and 4). Examination of Fig. 12 shows significant vorticity surrounding the bubble which can cause a shear-induced lift force to drive the bubble towards the wall. In general, the magnitude and direction of the measured transverse forces necessary for the observed migration are qualitatively consistent with the shear-induced lift forces observed by Sridhar and Katz.[14] This suggests that lift is primarily responsible for the wall peaking. Quantitative lift measurements are discussed in the next section.

For bubbles which eventually migrated toward the wall (i.e., were trapped), the typical sequence of events (based on the bubble trajectories and the liquid PIV vectors) was as follows: (1) Starting from injection, bubbles would disperse laterally in the turbulent boundary layer until a sufficiently strong vortex yielded a high lift force which caused them to collide with the wall; (2) at the point of initial impact, the bubbles would typically bounce away from the wall with a coefficient of restitution of approximately 0.8–0.9 for the first few bounces; (3) after several bounces, the bubbles' proximity to higher mean vorticity levels caused them to eventually slide (else they were ejected back into the boundary layer); and (4) the bubbles would then slide for a long period and could be ejected only occasionally (due to a strong uplifting vortex based on PIV images)—this ejection either resulted in a new set of bounces or allowed the bubbles to be ejected completely from the near-wall area. This sequence is thought to be primarily responsible for the near-wall peaking described above. The observed motions (2) and (3) were also experimentally observed[38] for a bubble of diameter 0.80 mm rising in a stagnant fluid near a vertical wall. However, a larger ellipsoidal bubble of diameter 1.76 mm yielded a larger bouncing amplitude which did not dissipate significantly, i.e., the bouncing continued to repeat. This phenomenon was found to be very similar to the interaction of two bubbles rising together at the same elevation, whereby the smaller spherical bubbles would coalesce or bounce a few times and coalesce later, while the larger deformable bubbles would bounce such that their separation distance increased from the original value.

D. Bubble forces in the turbulent boundary layer

For individual force measurements, bubble diameters of 0.42, 0.55, and 0.82 mm were introduced in the boundary layer with a free stream velocity of 0.4 m/s, and 0.58 mm diameter bubbles were investigated with a free stream velocity of 0.6 m/s. Computing the lift and drag forces acting on bubbles as described in (1) requires knowledge of the bubble position, bubble velocity, bubble acceleration, liquid velocity, and liquid acceleration. A sample time trace of the bubble velocity, liquid velocity and bubble relative velocity for a 0.55 mm bubble is shown in Fig. 13. From this, it is clear that a single bubble will experience a variety of Re_B values as it rises in the turbulent flow.

The relative strength of lift, drag, buoyancy, and stress gradient forces were calculated from such time histories. Recall that the stress gradient force is associated with the fluid acceleration $(D\mathbf{V}_F/Dt)$. The mean of the absolute values of these force components for the 0.82 mm diameter bubbles for each are shown in Fig. 14. This averaging method was employed in order to highlight the importance of forces with no preferred direction (e.g., the stress gradient force). These quantities are qualitatively in agreement with relative force strength analysis for the other bubble sizes. As expected the most important liquid forces were the buoyancy and drag forces, while the weakest was the stress gradient term. The rather significant lift force (compared to drag) is more consistent with magnitudes suggested by the Sridhar and Katz[14] formulation than by the Auton *et al.*[16] formulation (which would have predicted lift as only a few percentage points of the drag).

The instantaneous drag coefficients for several bubble trajectories were obtained for the above test conditions. In Fig. 15, the instantaneous drag coefficient data and a corresponding curve fit are plotted versus the bubble Reynolds number for the sample case of $d_B = 0.55$ mm. While there is significant experimental scatter (in line with the expected uncertainties), the drag coefficient consistently decreases with increasing Re_B for a fixed bubble diameter. This trend was found for all the bubble diameter curve fits, which are given in Fig. 16. Also shown in Fig. 16 are the results obtained by Sridhar and Katz[14] for contaminated bubbles $(0.5\ \mathrm{mm} < d_B < 0.8\ \mathrm{mm})$ entrained in a laminar vortex as well as the results from Clift *et al.*[19] for clean bubbles rising in still water. One can observe that present drag coefficient data values are approximately between the clean and contaminated conditions. This is consistent with the result that the quiescent rise velocity data for the present filtered tap water conditions lay in between that of previous clean and contaminated flow experiments.[25]

In addition to this generally expected behavior, there is significant variation in the C_D curve as a function of bubble

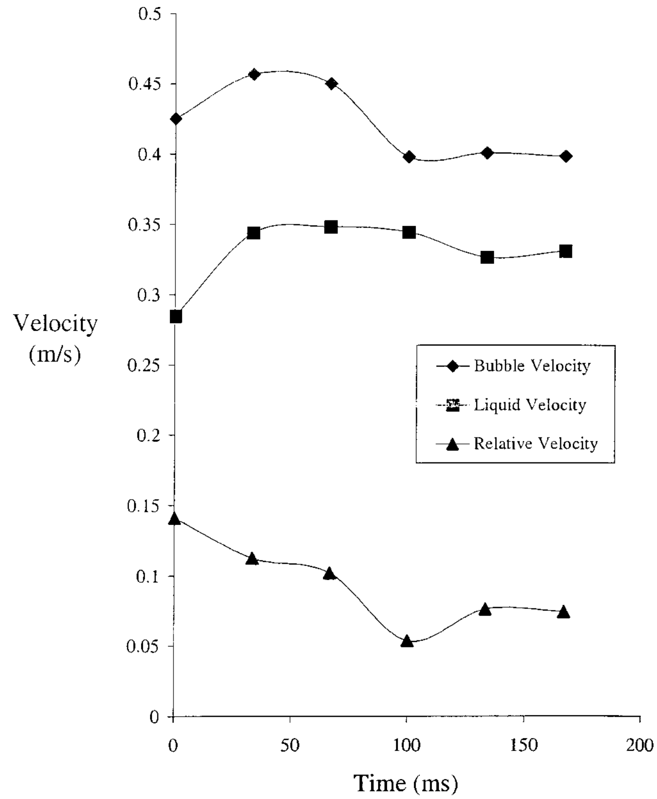

FIG. 13. Sample time trace of the vertical (streamwise) components of velocity for a 0.55 mm diameter bubble with $U_o = 0.4$ m/s ($\mathrm{Re}_\delta = 13\,000$).

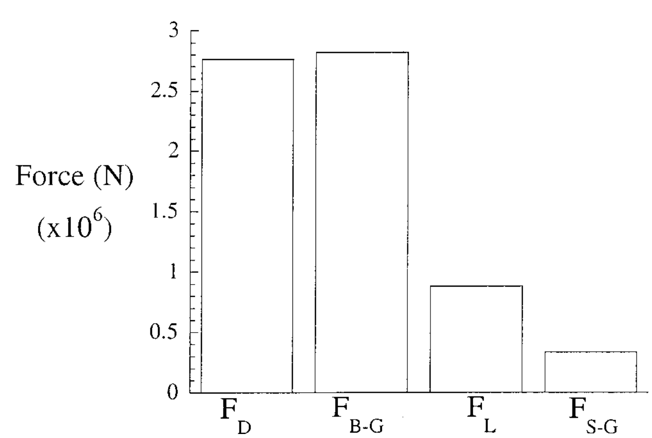

FIG. 14. Mean of the absolute value of liquid force components acting on a 0.82 mm bubble introduced in the 0.4 m/s free stream liquid velocity.

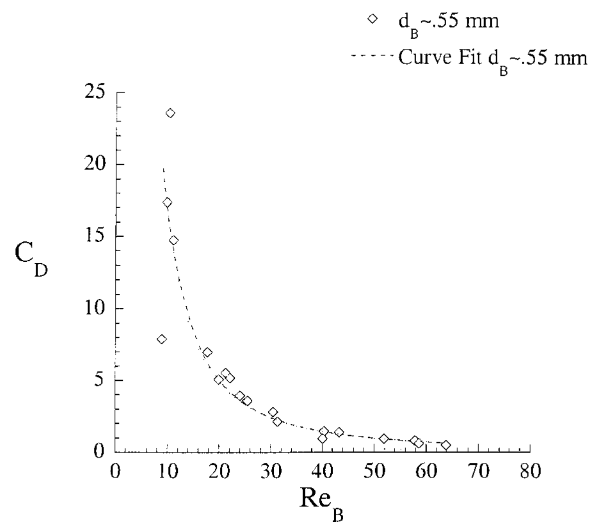

FIG. 15. Drag coefficient data and curve fit for the 0.55 mm diameter bubbles introduced in the liquid turbulent boundary.

diameter. This is unlikely to be caused by variation in the present nondimensional shear-rate values since this range has been found to have an insignificant effect on the drag coefficient.[39] Empirically it was noted that the present results indicate consistently decreasing C_D as turbulence intensity (relative to terminal velocity) increases for a fixed Re_B. This trend is congruent (qualitatively and quantitatively) with the phenomenon of increased rise velocity (and thus decreased mean drag coefficient) for bubbles subjected to turbulence as observed in experimental studies by Bataille *et al.*[20]

However, as mentioned in the Introduction, there have also been observations of decreased mean relative rise velocity (as compared to quiescent conditions) for turbulent conditions. To give further insight as to why both increases and decreases may occur, it is first important to note that there may be two competing but different mechanisms for modifying the mean rise velocities of bubbles in turbulent flow.

For the first mechanism, turbulence may reduce the *instantaneous* drag coefficient of a bubble for a given Reynolds number, i.e., it can lead to a modification of the C_D vs Re_B curve—this is the result found in the present measurements with turbulent intensities of 12%–33% of the rise velocity. This modification could then cause the mean terminal rise velocity to be higher than that in quiescent conditions—a result noted in the Bataille *et al.* experiments. In particular, they measured an increase of about 10% in mean bubble rise velocity for a turbulence intensity of about 6% of the rise velocity.

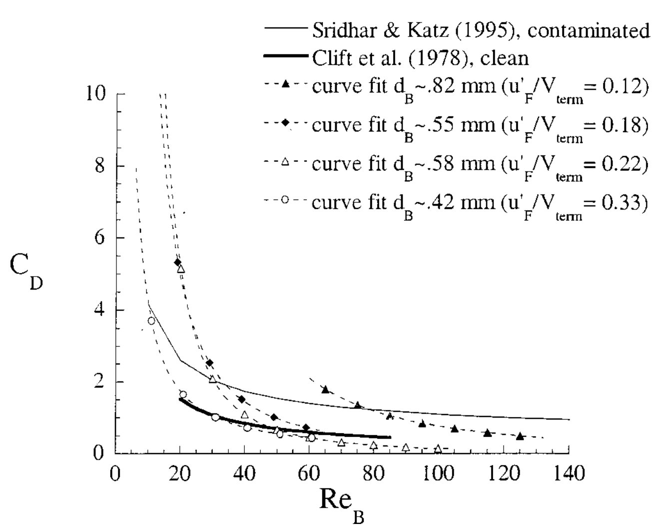

FIG. 16. Drag coefficient for 0.42, 0.55, 0.58, and 0.82 mm diameter bubbles introduced in the liquid turbulent boundary. These data are compared with Clift *et al.* (1978) and Srihdar and Katz (1995).

For the second mechanism, preferential location of bubbles to vortices may occur in which more down flow fluctuations than upflow fluctuations are seen at the bubble location owing to the unique bubble-eddy interaction dynamics. For a *fixed* C_D vs Re_B relationship, this mechanism may cause bubbles to see (on average) a net downward flow relative to the mean fluid velocity. This could then cause the mean terminal rise velocity to be lower than that in quiescent conditions. The net flow bias and the resulting change in terminal velocities were obtained with direct numerical simulations (DNS) with a fixed C_D-Re_B relationship by Wang and Maxey[40] for particles (which exhibited a terminal velocity increase) and by Maxey[18] for bubbles (which yielded a terminal velocity decrease). In both cases, it was found that the effect was primarily significant for bubble response times on the order of the Kolmogorov time scale. This effect was further established with numerical predictions of bubbles by Spelt and Beisheuvul[17] which employed Fourier series fluctuation with various assumed energy spectrums and a fixed linear drag law relationship. Their predictions yielded a decrease in terminal velocity for bubbles on the order of the Taylor microscale.

As such, both increases and decreases in mean rise velocity due to turbulence can occur depending on the test conditions. If both effects are occurring, a measurement of the mean rise velocity of bubbles in turbulence (as compared to quiescent conditions) can only determine which is dominating, but cannot quantify the individual effects. The experimental data of Poorte[21] was for bubbles about three times the Kolmogorov length scale, and showed both increases and decreases (though more of the latter occurred) of rise velocity due to turbulence. The decreases were attributed to the second mechanism, whereas the first mechanism may have been responsible for the increases. It should also be kept in mind that the uncertainties in the present measured drag coefficients were substantial and thus the results are primarily qualitative with respect to the correlation with turbulence levels. Thus, additional investigation is needed to confirm this behavior and to investigate for which test conditions it might be present.

Mean lift coefficients in the present turbulent flow were also computed based on the same trajectories. For each bubble size, the average lift coefficient ($\overline{\mathbf{C}_L}$) was computed along with the average nondimensional vorticity. The results are shown in Fig. 17 along with the experimental bubble data of Sridhar and Katz[14] and Narciri[22] and a C_L (with significant uncertainty) for a single particle trajectory from Van der Geld.[41] Also shown is the empirical C_L curve from Sridhar and Katz,[14] the theoretical predictions for inviscid flow, and the theoretical (creeping flow) predictions for Saffman lift at

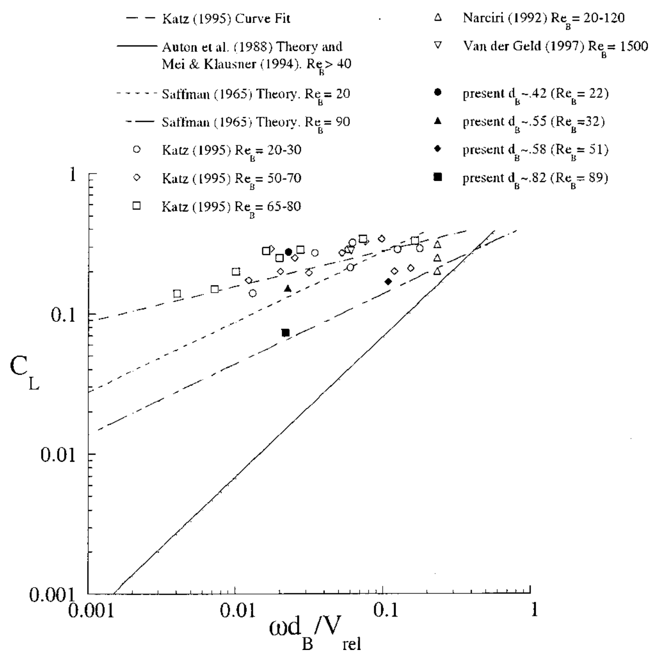

FIG. 17. Average lift coefficient vs average nondimensional vorticity for the present data and comparison with previous experimental and theoretical lift force studies.

$Re_B=20$ and 90. In general, all the experimental data points are consistently higher than the inviscid predictions, primarily lie in a single band, and are typically lower-bounded by the creeping flow predictions. This indicates that lift at moderate Reynolds numbers (Re_B of 20–120) can be quite substantial.

In addition, the present data for turbulent flow shows the lift coefficient decreasing with increasing Re_B, which is qualitatively consistent with the trends of Naciri[22] for a similar Re_B range but at higher $d_B\omega_F/V_{\mathrm{rel}}$ values. The qualitative trend is also consistent with that given by the Saffman[42] theoretical results (but which are intended for $Re_B \ll 1$). The quantitative differences with the Saffman theory can be partially explained by the significant uncertainty of the present lift coefficient measurements. However, Sridhar and Katz[14] results did not find any significant dependence on Re_B, which of course is also the case for the inviscid theory of Auton *et al.*[14] It is difficult to determine the specific cause of the difference between the Sridhar and Katz results and that of the present study with respect to Reynolds number influence. This difference could stem from the presence of turbulence for the present conditions, which may have modified the wake structure to some extent. If this is the case, one would expect decreasing relative turbulence intensity (via larger diameter bubbles) to give results which tend closer (and eventually asymptote) to the Sridhar and Katz laminar flow measurements. However, the present results actually show an increased departure to the laminar measurements as relative turbulent intensity decreases (albeit they become closer to the creeping flow predictions). Moreover, the Narciri data was for a laminar flow but showed an Re_B effect.

Perhaps a more likely mechanism for the present observed variation in lift coefficient at constant $d_B\omega_F/V_{\mathrm{rel}}$ is the variation in the slip condition at the particle–fluid interface, whereby increased slip can significantly reduce the predicted viscous lift force.[39] The contamination level and drag force results of Sridhar and Katz suggest a no-slip condition can be reasonably assumed, and obviously the Van der Geld result is for a no-slip condition. However, the present bubbles and those of Naciri are expected to have significant internal circulation (finite-slip) based on the increased quiescent terminal velocities as compared to typical contaminated values.[22,25] In general, the internal circulation effect can be expected to increase with bubble diameter, which is consistent with the trends of the present data and those of Naciri and also with their departure from the data of Sridhar and Katz and Van der Geld. However, further data and research is necessary to confirm this hypothesis and quantify the general lift relationship for spherical bubbles in turbulence for a variety of contamination levels.

IV. CONCLUSIONS

A vertical turbulent boundary layer in a water tunnel was employed to investigate distribution and motion of a dilute suspension of spherical bubbles. The test conditions included a filtered tap-water flow with $Re_\delta=13\,000-20\,000$ and bubbles with $Re_B=10-120$.

Inspection of the void fraction profiles yielded four distinct shapes, ranging from all bubbles trapped along the wall to all bubbles along or outside the edge of the boundary layer. The former shape was due to higher-Stokes conditions and higher shear-induced lift forces associated with the large diameter spherical bubbles. Lower-Stokes conditions (smaller diameter bubbles) at the same injection location resulted in the bubbles behaving nearly as passive scalars and diffusing throughout the boundary layer. Injection location dominated the peak void fraction position for bubbles that were not trapped along the wall. In general, the bubbles exhibited three basic types of individual trajectories: sliding, bouncing, and free-dispersion bubbles.

Drag and lift liquid forces on individual bubbles were obtained using time-evolving PIV vector fields, but with some experimental uncertainty. Analysis of the drag measurements indicates C_D decreases with increasing Re_B, as expected and which is consistent with previous quiescent and laminar flow data. However, there were variations for different bubble diameters, where decreasing C_D values tended to coincide with increasing turbulence intensity for an equivalent Re_B. The averaged lift forces were found to be qualitatively consistent in magnitude with previous laminar flow experiments. With respect to inviscid thoeretical predictions, the experimental results are much greater in magnitude. However, with respect to Saffman lift predictions (based on creeping flow theory), the present results indicate similar magnitudes, as well as the same reduction in lift coefficient with increasing Re_B.

ACKNOWLEDGMENTS

This work was supported by the Office of Naval Research under Grant No. N00014-96-1-0312. Anthony Flores also provided valuable experimental assistance.

[1]A. Serizawa, I. Kataoka, and I. Michiyosi, ''Turbulence structure of air–water bubbly flows: Part I–III,'' Int. J. Multiphase Flow **2**, 221 (1975).
[2]R. A. Herringe and M. R. Davis, ''Structure development of gas–liquid mixture flows,'' J. Fluid Mech. **73**, 97 (1976).
[3]V. E. Nakoryakov, O. N. Kashinsky, A. P. Burdukov, and V. P. Odnoral, ''Local characteristics of upward gas–liquid flows,'' Int. J. Multiphase Flow **7**, 63 (1981).
[4]R. van der Welle, ''Void fraction, bubble velocity and bubble size in two-phase flow,'' Int. J. Multiphase Flow **11**, 317 (1985).
[5]S. W. Beyerlein, R. K. Cosman, and H. J. Ritcher, ''Prediction of bubble concentration profiles in two-phase flow,'' Int. J. Multiphase Flow **11**, 629 (1985).
[6]L. Michiyosi, A. Serizawa, O. Takashi, K. Gakuhari, and T. Ida, ''Heat transfer and hydraulics of liquid metal-gas two phase magneto-hydrodynamic flow,'' Proceedings of the 8th International Heat Transfer Conference, San Francisco, CA, 1986.
[7]S. K. Wang, S. J. Lee, O. C. Jones, and R. T. Lahey, ''3-D turbulence structure and phase distribution measurements in bubbly two-phase flows,'' Int. J. Multiphase Flow **13**, 327 (1987).
[8]T. J. Liu, ''Bubble size and entrance length effects on void development in a vertical channel,'' Int. J. Multiphase Flow **13**, 309 (1993).
[9]K. Sekoguchi, H. Fukui, and Y. Sato, ''Flow characteristics and heat transfer in vertical bubble flow,'' in *Two-Phase Flow Dynamics*, edited by A. E. Bergles and I. Seikan (Kobe, Japan, 1981), pp. 59–74.
[10]E. Moursali, J. L. Marie, and J. Bataille, ''An upward turbulent bubbly boundary layer along a vertical flat plate,'' Int. J. Multiphase Flow **21**, 107 (1995).
[11]M. Lance and J. Bataille, ''Turbulence in the liquid phase of a uniform bubbly air–water flow,'' J. Fluid Mech. **222**, 95 (1991).
[12]S. Tran-Cong, J. L. Marie, and R. J. Perkins, ''Experimental study of the bubble dispersion in a turbulent boundary layer,'' ASME Fluids Engineering Division Summer Meeting, Vancouver, BC, 1997.
[13]C. Merkle and S. Deutsch, ''Microbubble drag reduction in liquid turbulent boundary layers,'' Appl. Mech. Rev. **45**, 103 (1992).
[14]G. Shridar and J. Katz, ''Drag and lift forces on microscopic bubbles entrained by a vortex,'' Phys. Fluids **7**, 389 (1995).
[15]B. Ford and E. Loth, ''Forces on ellipsoidal bubbles in a turbulent free shear layer,'' Phys. Fluids **10**, 178 (1998).
[16]T. R. Auton, J. C. Hunt, and M. Prud'Homme, ''The force exerted on a body in inviscid unsteady non-uniform rotational flow,'' J. Fluid Mech. **197**, 21 (1988).
[17]P. O. M. Spelt and A. Biesheuvul, ''On the motion of gas bubbles in homogeneous isotropic turbulence,'' J. Fluid Mech. **336**, 221 (1997).
[18]E. Loth, ''Numerical approaches for motion of dispersed bubbles, particles and droplets,'' Progress for Energy and Combustion Systems **26**, 161 (2000).
[19]R. Clift, J. R. Grace, and M. E. Weber, *Bubbles, Drops and Particles* (Academic, New York, 1978).
[20]J. Bataille, M. Lance, and J. L. Marie, ''Some aspects of the modeling of bubbly flows,'' *Phase-Interface Phenomena in Multiphase Flow*, edited by G. F. Hewitt, F. Mayinger, and J. R. Riznic (Hemisphere, New York, 1991).
[21]R. E. G. Poorte, ''On the motion of bubbles in active grid generated turbulent flows,'' Ph.D. thesis, University of Twente, The Netherlands, 1998.
[22]A. Naciri, ''Motion of gas bubbles in a turbulent and rotating fluid,'' Ph.D. thesis, 1992.
[23]R. Mei and J. F. Klausner, ''Shear lift force on spherical bubbles,'' Int. J. Heat Fluid Flow **15**, 62 (1994).
[24]D. Legendre and J. Magnaudet, ''The lift force on a spherical bubble in a viscous linear shear flow,'' J. Fluid Mech. **368**, 81 (1998).
[25]K. Felton, ''A study of spherical bubbles in a vertical turbulent boundary layer,'' Ph.D. thesis, Department of Aeronautical and Astronautical Engineering, University of Illinois at Urbana-Champaign, IL, 1999.
[26]A. L. Braslow, R. M. Hicks, and R. V. Harris, ''Use of grit-type-boundary layer-transition trips,'' NASA SP-124, 1966.
[27]W. C. Park, J. F. Klausner, and R. Mei, ''Unsteady forces on spherical bubbles,'' Exp. Fluids **19**, 167 (1995).
[28]H. N. Oguz and A. Prosperetti, ''Dynamics of bubble growth and detachment from a needle,'' J. Fluid Mech. **257**, 111 (1993).
[29]B. Ford and E. Loth, ''Diffusion of ellipsoidal bubbles in a turbulent shear layer,'' Int. J. Multiphase Flow **26**, 503 (2000).
[30]J. B. Young and T. J. Hanratty, ''Trapping of solid particles at a wall in a turbulent flow,'' AIChE J. **37**, 1529 (1991).
[31]R. D. Keane and R. J. Adrian, ''Optimization of particle image velocimeters. Part II: Multiple-pulsed,'' Meas. Sci. Technol. **2**, 963 (1991).
[32]G. Shridar and J. J. Katz, ''Implementation of particle image velocimetry to multiphase flow,'' Cavitation and Multi-phase Flow Forum **109**, 205 (1991).
[33]C. D. Meinhart, ''Investigation of turbulent boundary-layer structure using particle imaging velocimetry,'' Ph.D. thesis, University of Illinois, 1994.
[34]S. Okamato, ''Artificial thickening turbulent boundary layers,'' *Encyclopedia of Fluid Mechanics*, Vol. 8, edited by N. P. Cheremisinoff (Gulf, Houston, 1986), pp. 639–703.
[35]C. Tomkins, ''A particle image velocimetry study of coherent structures in a turbulent boundary layer,'' M.S. thesis, University of Illinois at Urbana-Champaign, IL, 1997.
[36]P. S. Klebanoff, NACA Tech. Notes No. 3178, 1954.
[37]J. L. Marie, E. Moursali, and M. Lance, ''A first investigation of a vertical bubbly flow past a flat plate,'' Proceedings of the First ASME/JSME Meeting on Fluid Mechanics, Portland, OR, 1991.
[38]L. van Wijngaarden, ''On pseudo-turbulence,'' Theor. Comput. Fluid Dyn. **10**, 449 (1998).
[39]S. Takgi and Y. Matsumotot, ''Numerical investigation of the lift force acting on bubbles and particles,'' ASME Fluids Engineering Division Summer Meeting, San Francisco, CA, FEDSM99-7848, 1999.
[40]L-P. Wang and M. Maxey, ''Settling velocity and concentration distribution of heavy particles in homogeneous isotropic turbulence,'' J. Fluid Mech. **256**, 27 (1993).
[41]C. W. M. Van der Geld, ''Measurement and prediction of solid sphere trajectories in accelerated gas flow,'' Int. J. Multiphase Flow **23**, 357 (1997).
[42]P. G. Saffman, ''The lift on a small sphere in a slow flow,'' J. Fluid Mech. **22**, 385 (1965).